Forest Fire Discrimination Based on Angle Slope Index and Himawari-8

Pingbo Liu and Gui Zhang *

Posted Date: 1 October 2024

doi: 10.20944/preprints202410.0009.v1

Keywords: Forest fire discrimination; Angle slope index; Himawari-8; decomposed three-dimensional OTSU

 doi:10.20944/preprints202410.0009.v1

Article

Forest Fire Discrimination Based on Angle Slope Index and Himawari-8

Pingbo Liu [1,2] and Gui Zhang [1,*]

[1] College of Forestry, Central South University of Forestry and Technology, Changsha 410004, China
[2] College of Computer Science and Mathematics, Central South University of Forestry and Technology, Changsha 410004, China
* Correspondence: zgui@csuft.edu.cn

Abstract: In the context of high frequency and intensity forest fires driven by future warming and drying climate, early detection and effective control of fires are extremely important to reduce losses. Satellite remote sensing, characterized by its broad observational scope and strong repeat observation capability, has become an important method for rapid monitoring of forest fires, replacing traditional means such as manual measurement and aerial photography. This paper addresses the misjudgments caused by solely relying on changes in infrared band brightness values and single-band separation in forest fire discrimination. It constructs the angle slope index ANIR based on the red band, near-infrared band and short-wave infrared band, Angle slope index AMIR based on the short-wave infrared band, mid-infrared band and far-infrared band, and angle slope index AMNIR based on the difference between the AMIR and ANIR, integrating the strong inter-band correlations and the reflectance characteristics of visible and short-wave infrared bands to simultaneously monitor smoke and fuel biomass changes in forest fires. To address the omissions caused by single-image fire discrimination algorithms, the paper constructs time-series Angle slope difference indices ΔANIR and ΔAMIR. To address the different fire point discrimination thresholds caused by background difference in different time and space, the paper uses the decomposed three-dimensional OTSU(Maximum inter-class variance method) algorithm to calculate the segmentation threshold of the sub-regions constructed from the AMNIR data. The methods were validated using high temporal resolution meteorological satellite Himawari-8 and ground truth fire data from Hunan Province, China, from 2018-2019. The results show that the discrimination method based on the ASITR(Angle slope indices thresholds) method exhibits an accuracy of 0.88, a missed detection rate of 0.17, and an overall evaluation value of 0.85, which is 0.09 higher in accuracy and 0.03 higher in overall evaluation than the discrimination method based on infrared bands brightness values proposed by Feng et al. [1] (accuracy 0.79, missed detection rate 0.14, overall evaluation value 0.82); the method based on the FAMN_OTSU_ASITR (Fusion of Angle slope difference index ($AMNIR$) data, Decomposed three-dimensional OTSU adaptive threshold segmentation Algorithm and ASITR) exhibits an accuracy of 0.85, a missed detection rate of 0.08, and an overall evaluation value of 0.88, which is 0.09 lower in missed detection rate and 0.03 higher in overall evaluation as compared to the ASITR. The results demonstrate that the forest fire discrimination method based on Angle slope indices, Himawari-8 satellite data, and the decomposed OTSU adaptive threshold segmentation algorithm can improve the accuracy of forest fire discrimination and reduce errors in missed detections.

Keywords: Forest fire discrimination; Angle slope index; Himawari-8; decomposed three-dimensional OTSU

1. Introduction

Forest fire has been listed by the United Nations as one of the biggest threats to social crises and ecological disasters [2]. It is one of the biggest threats to forest resources and ecological civilization construction and can destroy millions of acres of land at shockingly fast speeds. The duration of fire seasons globally has extended by 27% since 1979, and the severity has multiplied. It was reported that with global warming of 1.5°C, the world would face inevitable multiple climate hazards, and even temporarily exceeding this warming level will cause additional severe impacts, some of which

 doi:10.20944/preprints202410.0009.v1

will be irreversible [3].This means that the fire prevention situation is extremely serious in the coming years.

In the context of high frequency and intensity forest fires driven by future warming and drying climate, early detection and effective control of fires are extremely important to reduce losses resulting from forest fires. Satellite remote sensing, which is characterized by a wide observation and strong repeat observation capability, has become an important means of rapid monitoring of forest fires, replacing traditional means such as manual measurement and aerial photography [4]. It has significant advantages over fires occurring in pristine forest areas that are difficult to access [5].

Many scholars have made use of remote sensing data to study forest fire identification [6–23]. The Cooperative Institute for Meteorological Satellite Studies developed the Visible Infrared Spin Scan Radiometer Atmospheric Sounder(VAS) automated biomass burning algorithm(ABBA) to automatically detect and characterize active fires. Prins et al. wrote the Algorithm Theory Document of COESRABI Fire Point Recognition(ATBD) based on the ABBA [13], however, the fire detectability and characterization was limited by the relatively coarse spatial resolution of the Geostationary Operational Environmental Satellite(GOES) VAS instrument. Dozier used the mid-infrared band for fire monitoring and proposed a sub-pixel fire point estimation model based on Planck's law [10], which was improved by many subsequent algorithms [14–16]. Kaufman and others proposed the MODIS fire point detection algorithm based on the Advanced Very High Resolution Radiometer(AVHRR) global fire point detection algorithm [17,18], which, after revision by Justice et al. [19], was used for global fire monitoring product production. However, it was found that this algorithm exhibits serious misjudgments in sparsely vegetated areas and missed detections of low brightness small fire points. Giglio et al. [20] further revised it in 2002, improved an contextual active fire detection algorithm based on both the 4 μm brightness temperature and the 4 μm and 11 μm brightness temperature difference which offered increased sensitivity to smaller, cooler fires as well as a lower false alarm rate. Chinese researchers also conducted related research using MODIS for fire monitoring and proposed a new detection index K ((T20-T31)/T20) [21,22]; Gong et al. used the Breaks for Additive Segments and Trend (BFAST) algorithm to detect breakpoints of time series data and identify potential fire points to address the deficiency associated with the fixed threshold discrimination method which could not meet regional differences [23].

Furthermore, to address the poor universality of threshold and contextual methods, scholars have introduced time series detection methods and machine learning algorithms (Support Vector Machine (SVM), decision tree models, Random Forest classifiers (RF), Maximum inter-class variance method (OTSU) into existing discrimination algorithms [24–28]. While random forest classifiers achieved good discrimination results, they require input of different parameters for different research areas, and the volume of input parameters is large. Deep learning is limited by the size of the data for practical application. One-dimensional OTSU [29] and two-dimensional OTSU [30] cannot differentiate noise in the image close to the target; three-dimensional OTSU [31] algorithm has not been effectively used in practical applications due to high computational complexity and large amount of computation. At the same time, high temporal resolution new-generation geostationary meteorological satellites (such as Himawari-8) gradually replace older-generation polar orbiting and geostationary meteorological satellites (VIIRS [32], MODIS [33], GOES [34]), and becomes mainstream in the Eastern Hemisphere [35–41]. Xiong et al. [25,39,40] used data from Himawari-8 and FY-4A to build various models for forest fire discrimination and found that the decision tree model had the highest accuracy in fire discrimination, and the most suitable band combination for forest fire discrimination was 3.72 μm and 10.8 μm. Jang [41] developed a method for obtaining effective fire detection parameters, inputting various differences and ratios of Himawari-8 bands into a random forest classifier and selecting high-importance features. Feng et al. [1] used the ratio relationship between the value, mean value, and standard deviation of image pixels and developed a new index to distinguish potential fire points according to the brightness temperature changes of mid-infrared and thermal infrared when a fire occurred, and improved the discrimination accuracy.

However, the aforementioned forest fire monitoring methods are all based on infrared band brightness values and the indices constructed from them, ignoring the changes of other bands during

 doi:10.20944/preprints202410.0009.v1

forest fires and the strong inter-band correlations. Even with high temporal resolution geosynchronous satellite algorithms for early fire detection [43–45], fire detection is still performed by estimating the temperature of the background area to separate fire pixels. When forest fires occur, fire smoke, vegetation destruction, and thermal radiation changes can impact visible, near-infrared, and infrared bands, and there is a strong correlation between each independent band in the spectral imagery. The relationship between bands of different wavelengths in the spectral data is as important as the reflectance and brightness temperature value. Scholars have made some attempts in this area [24,46–50], proposing methods such as brightness temperature-vegetation index-aerosol optical depth method [45], brightness temperature-smoke fusion method [24,46], the solar zenith angle [47] etc. Wooster et al. constructed the fire point extraction index [48] of LSA SAF Meteosat satellite based on the brightness temperature of IR 3.9 μm (MWIR), IR 10.8 μm (LWIR) ,IR 12.0 μm (LWIR) channels and the spectral radians of IR 3.9 μm and VIS 0.6 μm (visible) channels based on the SEVIRI sensor of European Meteosat satellite. This method uses a lower threshold to avoid the missed detection of fire points as much as possible, but the pixel parameter value in the area uniformly heated by the sun may also reach the detection limit, leading to a large error. Pan et al. [49] considered the effects of the atmosphere and sun on smaller surfaces in daytime images and improved a more practical spectral method, but the method still could not produce corresponding effects in complex real environments.

To address the above problems, this paper constructs new indexes for forest fire discriminant which make full use of the spectral bands of satellite remote sensing images and the strong correlation between them, and adopt the decomposed 3-dimensional OTSU adaptive threshold segmentation algorithm according to the background differences in different regions at the same time, with a goal to improve the accuracy of fire point recognition.

The main contributions are as follows:

1. To address the misjudgments caused by solely relying on changes in infrared band brightness values and single-band separation for forest fire discrimination, the Angle slope index based on Mid-infrared (AMIR), Angle slope index based on Near- infrared (ANIR), and Angle slope index based on the difference between mid-infrared and near-infrared (AMNIR) were constructed. These indices integrate the reflectance characteristics of visible and short-wave infrared bands and the strong inter-band correlations, enabling simultaneous monitoring of forest fire smoke and fuel biomass changes. This approach enhances sensitivity and improves accuracy.
2. To address the variations in fire discrimination thresholds across different backgrounds, based on images constructed from Angle slope difference index AMNIR, a decomposed three-dimensional OTSU algorithm was employed to calculate the fire point discrimination thresholds for subregions of the study area. This adaptive threshold calculation method reduces the rate of missed detections in fire discrimination, simplifies algorithm complexity, and improves efficiency, making it suitable for more practical application.
3. To address the missed and incorrect detections caused by single-image fire discrimination algorithms, time-series remote sensing images were used to construct the time-series Angle slope difference indices ΔANIR and ΔAMIR, thus enhancing the accuracy of fire discrimination.

2. Data and Methods

2.1. Data

2.1.1. The Remote Sensing Satellite Sensors and Data Channels

Himawari-8 satellite was launched at 14:16 on October 7, 2014, equipped with the advanced imager AHI, the temporal resolution of the entire observation is 10 min once, and that of Japan and specific target areas can reach 2.5 min, the spatial resolution is divided into three section: 0.5km (channel 3), 1km (channel 1,2,4), and 2km (channel 5~16) [7]. The AHI has 16 detection channels: 3 visible light channels (red, green and blue), 3 near-infrared channels, 10 infrared channels, which can be used to detect various fields including surface vegetation, ocean water color, atmospheric environment, cloud parameters and fire point identification. As Himawari-8 satellite can accurately locate fire points within 1 pixel, it would meet the requirements in actual fire monitoring. The study

 doi:10.20944/preprints202410.0009.v1

data were full-scale observation data of Himawari-8 L1 NC (Network Common Data Format) downloaded from the Japan Meteorological Agency. After downloading, the data were pre-processed by channel extraction, brightness temperature calculation, cropping and other ways for forest fire discrimination.

This study also uses sentinel-2A data to observe and verify forest fires. The Sentinel-2A satellite, part of the "Global Environment and Security Monitoring" initiative, was launched on June 23, 2015. Sentinel-2A is equipped with a multispectral imager capable of covering 13 spectral bands with a swath width of 290 kilometers. It offers a spatial resolution of 10 meters and a revisit cycle of 10 days. The satellite features different spatial resolutions across the visible, near-infrared, and short-wave infrared spectra, and is used for observing changes in land cover and forests, monitoring pollution in lakes and coastal waters, and imaging natural disasters such as floods, volcanic eruptions, and landslides. Sentinel-2 data were downloaded from the European Space Agency's Copernicus Data Center (https://scihub.copernicus.eu/dhus/#/ home). The Level-1C product (raw data) was radiometrically corrected using Sen2Cor2.5.5 software [8] and converted to the Level-2A product. The Sentinel-2 images after preprocessing (mainly including geometric and atmospheric corrections) were UTM48 WGS84, with a re-sampling of 10m spatial resolution.

The remote sensing satellite sensors and data channels selected are shown in Table 1.

Table 1. Selected bands of Satellite imagery data set in this study.

Satellite	Sensor	Channel No.	Wavelength (μm)	Spatial Resolution (m)
Himawari-8	AHI	1	0.46	1000
		2	0.51	1000
		3	0.64	500
		4	0.86	1000
		5	1.60	2000
		6	2.30	2000
		7	3.90	2000
		8	6.20	2000
		14	11.20	2000
		16	13.30	2000
Sentinel-2A	MSI	2	0.49	10
		3	0.56	10
		4	0.665	10
		8A	0.865	20
		11	1.61	20
		12	2.19	20

2.1.2. Sample Points Data for Angle Slope Index Threshold Statistics

Australia, located in the southern hemisphere's hot zone, with a latitude and longitude range of 10°41' ~ 43°39', 112° ~ 154° (see Figure 1), has a dry climate with little annual rainfall. It has extensive forest cover, primarily consisting of flammable tree species. The forest fires in Australia are among the most powerful disasters in recent years, characterized by long durations and wide areas, causing severe environmental, economic, and social impacts. The hot, dry, and cloudless weather in Australia provides a unique advantage for the collection of forest fire sample points. In this study, the sample data were taken from Australia and selected based on historical news records and Himawari-8 satellite forest fire product data (Reliability=5) as shown in Table 2 and Figure 2. In the selection process, the fire sample information was verified by the fire smoke and burned area information on

 doi:10.20944/preprints202410.0009.v1

the satellite imagery combined with the band 3, band 2, band1 of Himawari-8 satellite and the band 4, band 3, band 2, band 12, band 11, band 8A of Sentinel-2 , as shown in Figure 3.

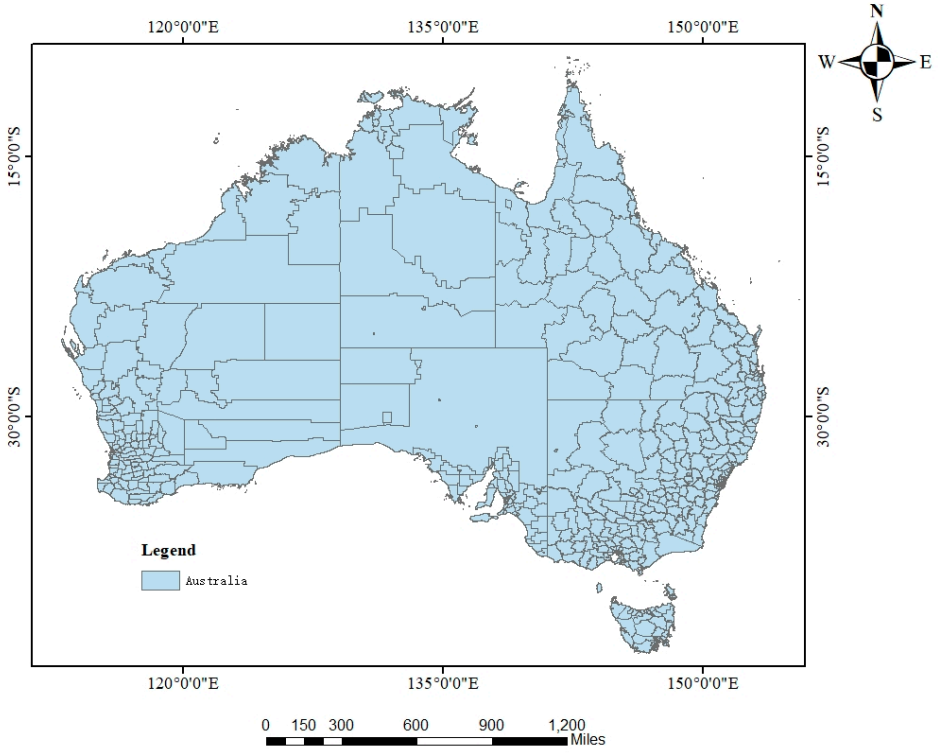

Figure 1. Area of Sample points data for angle slope index threshold statistics.

Table 2. Partial experimental data information of the Himawari-8.

Address	Type	Date & Time	Imagery	Level
West Australia (South East)	Fire point sample	May 2, 2022, 02：10 and 02：30	NC_H08_20220502_0200_R21_FLDK.06001_06001.nc	Level 1
			NC_H08_20220502_0210_R21_FLDK.06001_06001.nc	Level 1
			NC_H08_20220502_0230_R21_FLDK.06001_06001.nc	Level 1
			H08_20220502_0200_L3WLF010_FLDK.06001_06001.csv	Level 3
			H08_20150727_0800_L2WLF010_FLDK.06001_06001.csv	Level 3
	Forest land sample	March 12, 2022, 2：00	NC_H08_20220312_0200_R21_FLDK.06001_06001.nc	Level 1
West Australia (West South)	Fire point sample	February x, 2022, 00：00, 00：30, and 01：00	NC_H08_20220207_0000_R21_FLDK.06001_06001.nc	Level 1
			NC_H08_20220207_0030_R21_FLDK.06001_06001.nc	Level 1
			NC_H08_20220207_0100_R21_FLDK.06001_06001.nc	Level 1
			H08_20220207_0000_L3WLF010_FLDK.06001_06001.csv	Level 3
			H08_20220207_0100_L3WLF010_FLDK.06001_06001.csv	Level 3
	Forest land sample	December 17, 2021, 02：10	NC_H08_20211217_0210_R21_FLDK.06001_06001.nc	Level 1
West Australia (outside Perth)	Fire point sample	February 2, 2022, 03：00, 03：30 and 04：00	NC_H08_20210202_0300_R21_FLDK.06001_06001.nc	Level 1
			NC_H08_20210202_0330_R21_FLDK.06001_06001.nc	Level 1
			NC_H08_20210202_0400_R21_FLDK.06001_06001.nc	Level 1
			H08_20210202_0300_L3WLF010_FLDK.06001_06001.csv	Level 3
			H08_20210202_0400_L3WLF010_FLDK.06001_06001.csv	Level 3
	Forest land sample	December 7, 2020, 03：30	NC_H08_20201207_0330_R21_FLDK.06001_06001.nc	Level 1
New South Wales	Fire point sample	November 17, 2019, 00：30 and 01：00	NC_H08_20191117_0030_R21_FLDK.06001_06001.nc	Level 1
			NC_H08_20191117_0100_R21_FLDK.06001_06001.nc	Level 1
			H08_20191117_0000_L3WLF010_FLDK.06001_06001.csv	Level 3
			H08_20191117_0100_L3WLF010_FLDK.06001_06001.csv	Level 3

 doi:10.20944/preprints202410.0009.v1

	Forest land sample	September 11, 2019, 01：00	NC_H08_20200330_0550_R21_FLDK.06001_06001.nc	Level 1

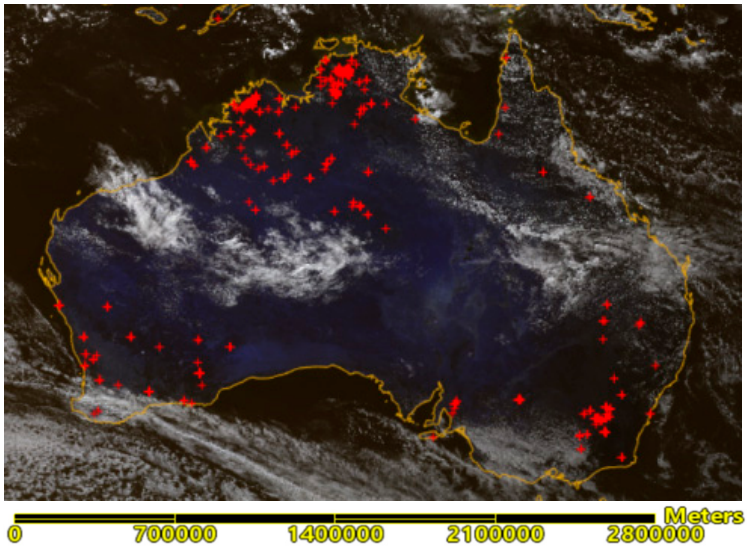

Figure 2. Location map of fire points and forest land sample points (the red points) taken in the study.

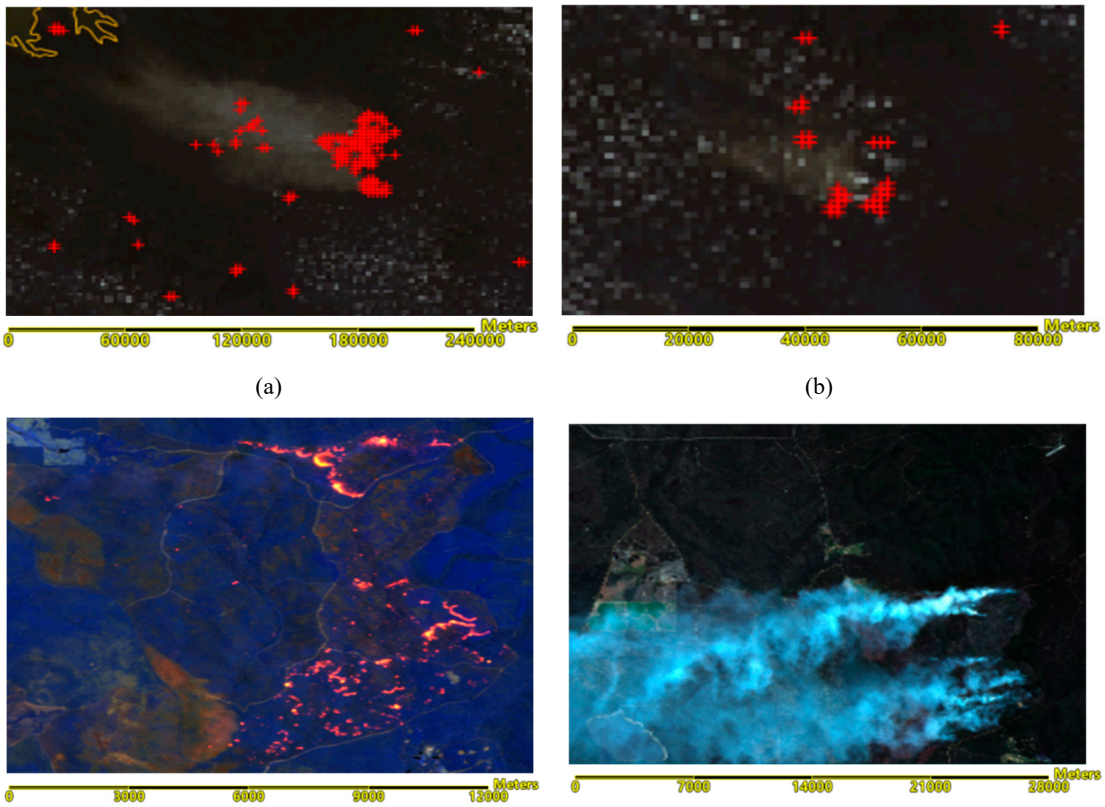

(a) (b)

(c) (d)

Figure 3. Fire point and smoke sample diagrams. (**a**)Example of fire point smoke (outside the city of Perth, Western Australia, 2/2/2021, 00:00); (**b**)Example of fire point smoke(Northern Australia, 5/2/2021, 05:00); (**c**)False-color composite image using bands 12, 11, 8A, near the Margaret River in Australia, 12/7/2021 02:13; (**d**)True-color composite image using bands 4, 3, 2, near the Margaret River in Australia, 12/7/2021, 02:13.

 doi:10.20944/preprints202410.0009.v1

2.1.3. Forest Fire Ground Actual Data and Land Cover Data

Hunan Province is located in the central of China, with a latitude and longitude range of 108°47′ ~ 114°15′, 24°38′ ~ 30°08′ (see Figure 4), a mountainous area of about 108,472 km², and a total land area of 211,829km², accounting for 51.21% of total land area [51]. It has a subtropical monsoon climate with abundant light, heat and precipitation, the average annual temperature in it ranges between 16°C ~ 18°C. The favorable climatic conditions resulted in dense vegetation, as of 2022, forest coverage rate in Hunan Province is 59.98% [52]. Due to large mountainous area and high forest cover, the situation of forest fire fighting work is critical. From 2000 to 2018, a total of 25,977 forest disaster fires occurred in Hunan Province, with a total victimized forest area of 1062.21km² and a total forest fire area of 1954.60km². Effective forest disaster fire monitoring and fighting are of practical significance in maintaining ecological security.

Forest fire actual data is provided by the Hunan Forest Fire Prevention and Extinguish Command Center after video verification and manual verification, and contain information such as location, forest fire initiation time, forest fire extinguish time, affected area, weather, forest fire initiation reason and so on.

The Hunan Forest Fire Prevention and Extinguish Command Center sends professional to confirm and report in detail on forest disaster fire occurred in Hunan Province. Professional utilize Global Position System(GPS), surveying equipment and CW-15 vertical take-off and landing fixed-wing drone(fuselage length 2.06m, wingspan 3.54m, endurance 180 min, cruise speed 61km/h, horizontal positioning accuracy 1cm+1ppm.), with CA-103 aerial camera(sensor size 35.70mm×23.80mm, effective pixels 61 megapixels, image resolution or pixels 9504×6336), to conduct on-site survey, post-disaster assessment, and wide-area orthophoto or tilt data collection.

Table 3 shows the information about a portion of the forest fire actual data.

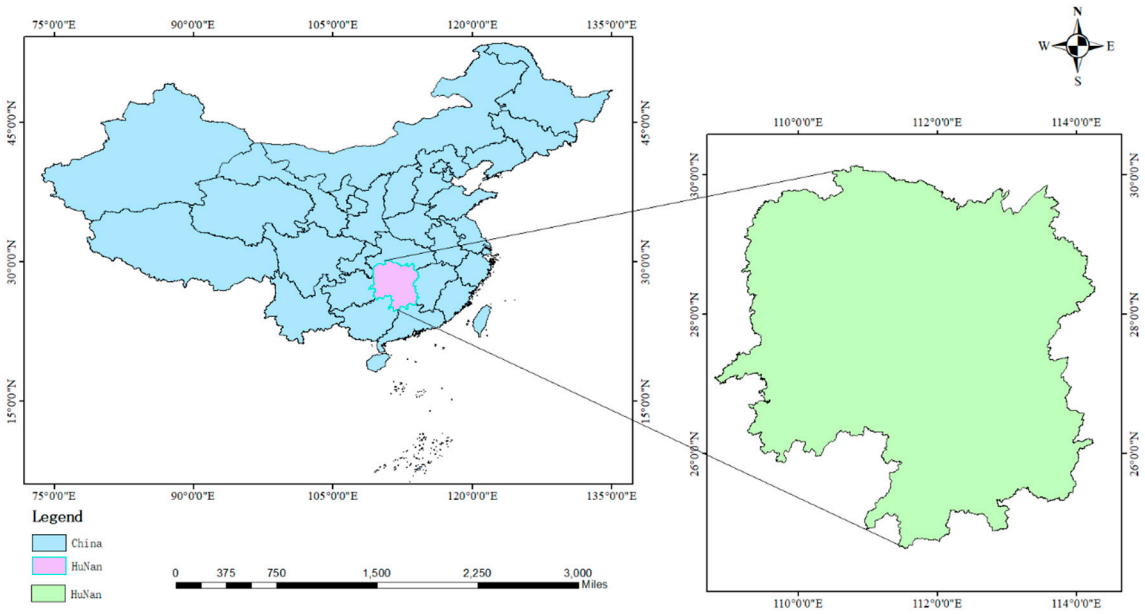

Figure 4. Area of Forest fire ground actual data.

Table 3. Time and location Information on the forest fire actual data.

No. *	Time of the Fire Event	Longitude	Latitude	Extent (ha)
1	October 6, 2018 at 05:00 UTC	109°52′	27°17′	95.88
2	September 28, 2019 at 07:20 UTC	109°36′	28°15′	34.00
3	September 28, 2019 at 05:30 UTC	109°34′	28°12′	22.00
4	September 28, 2019 at 03:10 UTC	111°19′	29°19′	0.87
5	March 20, 2020 at 08:00 UTC	109°23′	28°21′	8.4

 doi:10.20944/preprints202410.0009.v1

6	March 21, 2020 at 08:11 UTC	112°21′	26°19′	18.00
7	November 8, 2020 at 09:12 UTC	118°28′	27°13′	11.00
8	January 14, 2021 at 09:10 UTC	112°27′	26°43′	20.70
9	January 14, 2021 at 07:15 UTC	112°29′	27°8′	5.80
10	January 14, 2021 at 07:50 UTC	110°51′	26°51′	4.50
11	January 19, 2021 at 04:30 UTC	113°48′	25°49′	18.55
12	January 19, 2021 at 06:30 UTC	113°1′	25°41′	23.73
13	January 19, 2021 at 09:48 UTC	112°20′	26°12′	0.20
14	January 19, 2021 at 10:23 UTC	113°53′	28°55′	0.90
15	February 20, 2021 at 09:15 UTC	113°17′	25°38′	9.30

* No. = Number.

The Global Land Cover data with 30-meter resolution for 2017 were downloaded from the Star Cloud Data Service Platform of Peng Cheng Laboratory (https://data-starcl oud.pcl.ac.cn/zh). The data include eleven categories: farmland, forest, grassland, shrubland, wetlands, water bodies, tundra, impervious surfaces, bare land, ice and snow, and clouds.

The 30-meter Global Land Cover Fine Classification Product V1.0 for the year 2020 was downloaded from the Data Sharing Service System of the Aerospace Information Research Institute, Chinese Academy of Sciences. The land cover classification includes, but is not limited to, land use types (such as farmland, forests, urban areas), surface water bodies (such as lakes, rivers), rocks, and soils, encompassing a total of 29 categories. The forest areas within Hunan Province extracted from this data are shown in Figure 5.

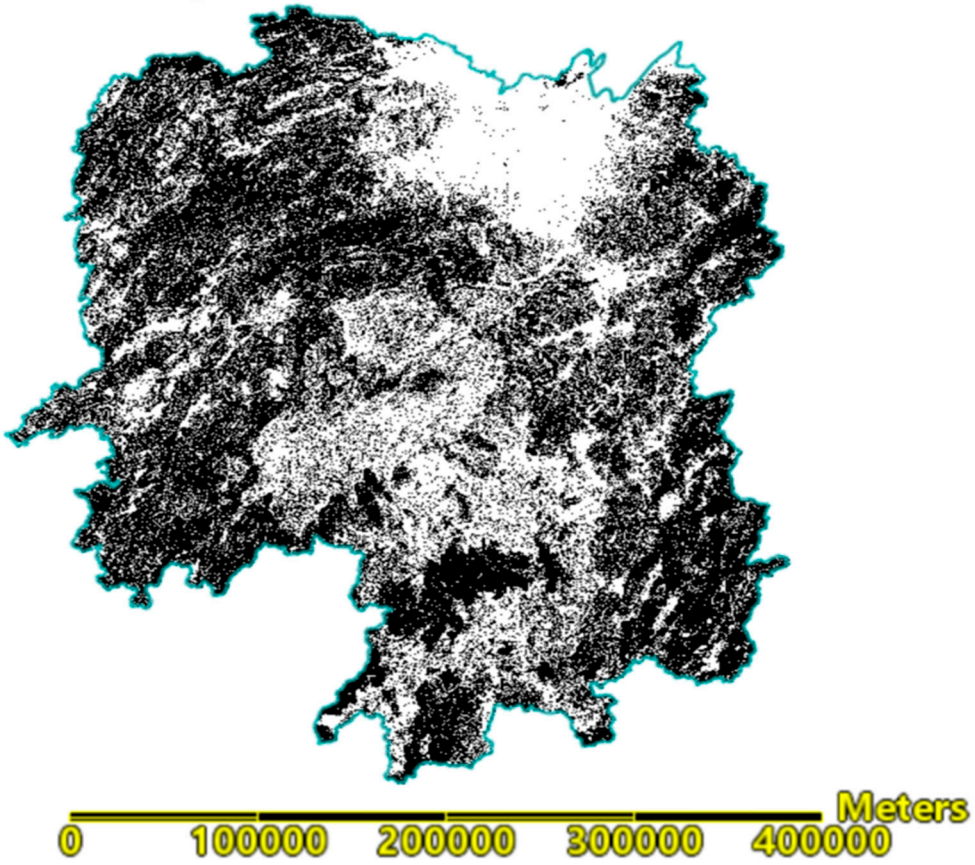

Figure 5. The forest area of 30m surface coverage in Hunan province in 2020 (black area).

2.2. Method

 doi:10.20944/preprints202410.0009.v1

The forest fire discrimination method based on the Angle slope index utilizes the unique characteristics of angles formed by reflectance values in visible, near-infrared, and short-wave infrared bands, as well as brightness temperatures in mid-infrared and far-infrared bands in the spectral images of forested areas and fire points. The method also leverages changes in these angles observed in spectral images during a fire event to construct a forest fire discrimination index. Additionally, a decomposed three-dimensional OTSU adaptive threshold segmentation algorithm is used to calculate the forest fire index thresholds against different backgrounds. The accuracy of this method is evaluated using actual forest fire data. Figure 6 illustrates the data processing and analysis flowchart, which will be elaborated in the subsequent sub-sections.

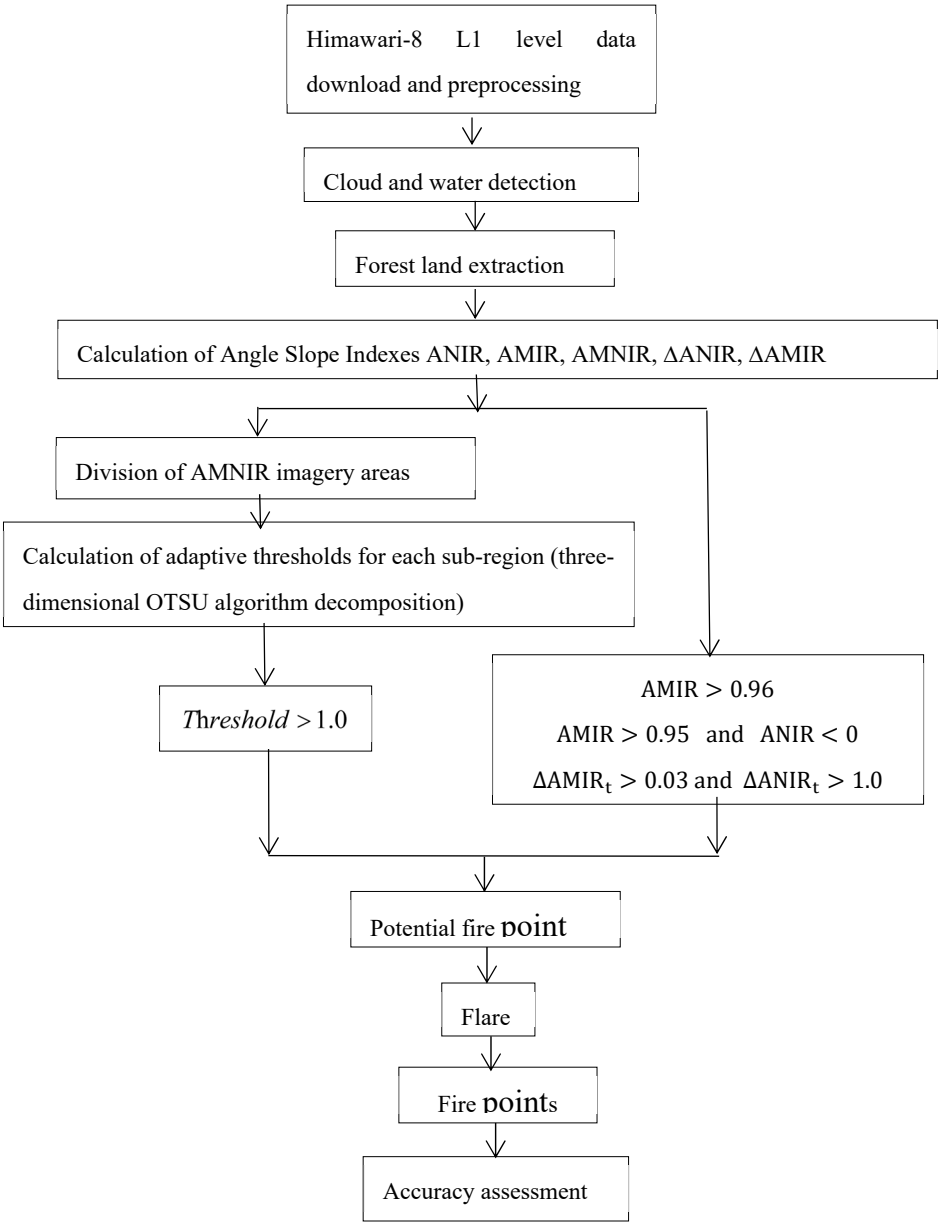

Figure 6. Flowchart for forest fire discrimination based on Angle Slope Indexes and Himawari-8.

2.2.1. The Theoretical Basis of Satellite Remote Sensing Fire Point Identification

When forest fires occur, vegetation in the burning area is destroyed, and the decrease of chlorophyll content causes changes in the reflectance of visible, red-edge and near-infrared (NIR) bands, which are specifically reflected in the reflectance of near-infrared band decreases, the short-wave infrared reflectance increases, and the normalized vegetation index ($NDVI = (NIR - R)/\ (NIR + R)$ decreases significantly. At the same time, according to the basic law of

 doi:10.20944/preprints202410.0009.v1

thermal radiation (Wien displacement law), the wavelength corresponding to the object's radiation peak is inversely proportional to the temperature, and as the object's temperature increases, the radiation peak moves to the shortwave direction. The main temperature range of forest burning is 600~1300 K, and the corresponding peak wavelength is in the mid-infrared (MIR, 3~5μm) range, while the peak wavelength of surface normal temperature (about 300K) is about 11μm. In the mid-infrared band, the difference between the radiation emitted by combustion and the background radiation can be up to four orders of magnitude. According to Planck's law, this difference in radiation brightness results in that even if the fire area only accounts for 1/104-1/103 of the total area of the pixel, the brightness temperature value of the fire point pixel in the mid-infrared band will be significantly increased, and there is a significant difference with the surrounding pixel. In the far infrared band, this difference in brightness temperature also occurs, but the difference is smaller. This characteristic of bright temperature difference can be used as the main basis for fire point identification.

2.2.2. Forest Fire Discrimination

2.2.2.1. Cloud Detection

Clouds obscure the real information of ground objects when monitoring forest fire with remote sensing imagery, and reduce the quality of image and the accuracy of fire point discrimination. In this study, a multi-spectral comprehensive threshold cloud detection algorithm is adopted. It uses the brightness temperature or reflectivity of clouds in infrared and visible spectrum to identify the characteristics different from other ground objects, and the detection results were corrected by clear sky repair algorithm. The specific algorithm is as follows:

Identify thick cloud conditions：

$$\rho 03 > 0.3 \quad \text{or} \quad 0.9 < \frac{\rho 04}{\rho 03} < 1.1, \tag{1}$$

Identify high cloud conditions：

$$BT_{16} < 236K \quad \text{or} \quad (0.09 < \frac{\rho 03 - \rho 05}{\rho 03 + \rho 05} < 0.2 \quad \text{and} \quad \rho 01 > 0.1), \tag{2}$$

Identify medium cloud conditions：

$$\mathrm{BT}_{14} < 278K \quad \text{or} \quad BT_7 - BT_{14} > 20K, \tag{3}$$

Perform clear sky repair on the identified cloud pixels:

$$-0.18 \le NDVI \le 0.2, \tag{4}$$

Where: ρ is the apparent reflectance of channels 3, 4, 5 of AHI, BT is the brightness temperature of channels 7, 14, 16 of AHI, NDVI is the normalized difference vegetation index.

2.2.2.2. Forest Land Discrimination

Considering the dynamic changes of forest resources, the following comprehensive methods are adopted in woodland identification:

1. Use land cover data: The product of Global Land Cover with Fine Classification System at 30m in 2020 downloaded from the website of Earth big data science engineering data sharing service system supported by the Institute of Aerospace Information Innovation, Chinese Academy of Sciences.
2. Use the Normalized Difference Vegetation Index (NDVI) to confirm:

$$NDVI = (NIR - R)/(NIR + R) \quad \text{and} \quad NDVI > 0.45, \tag{5}$$

where NIR represents the reflection value of the near infrared band, and R represents the reflection value of the red band.

 doi:10.20944/preprints202410.0009.v1

2.2.2.3. Forest Fire Point Discrimination

1. Construction of Angel slope Indices and forest fire discrimination.

The Angle slope index, proposed by Palacios-Orueta and Khanna et al., describes the relationship between the three continuous bands by using the geometric shape of the spectra, so it detects not only the reflectance values of bands, but also the relationship between the bands. When forest fires break out, vegetation destruction and thermal radiation have a certain impact on visible, near-infrared and infrared bands (see Figure 7). There is a strong correlation between each independent band in spectral images, and the relationship between bands in spectral data is as important as the reflectivity, radiation and brightness temperature. Therefore, the Angle slope index is more sensitive to the occurrence of forest fires and can better capture the information of forest fire points. In this study, new Angle slope indexes were constructed to analyze the spectrum characteristics and changes of forest fire points.

As shown in the schematic diagram of the spectral curve in Figure 7, the x-axis in the coordinate system represents the identifiers for bands 1-16 of the Himawari-8 satellite, corresponding to integer values 1-16. The y-axis corresponds to reflectance values for bands 1-6, which cover the visible, near-infrared, and short-wave infrared regions, while for bands 7-16, it corresponds to the brightness temperature values in the infrared region.

Angle slope indices ANIR , AMIR and AMNIR are defined as follows：

$$ANIR = \frac{|R_R R_N|^2 + |R_N R_S|^2 - |R_R R_S|^2}{2|R_R R_N||R_N R_S|}, \tag{6}$$

$$AMIR = \frac{|R_S R_M|^2 + |R_M R_F|^2 - |R_S R_F|^2}{2|R_S R_M||R_M R_F|}, \tag{7}$$

In formula (6), R_R , R_N respectively represent the points corresponding to the reflectance values of the red band and near-infrared band on a coordinate system, $|R_R R_N|$ represents the distance between these two points in the coordinate system, similarly, $|R_N R_S|$ represents the distance between the points corresponding to the reflectance values of the near-infrared band and short-wave infrared band in the coordinate system，$|R_R R_S|$ represents the distance between the points corresponding to the reflectance values of the near-infrared band and short-wave infrared band in the coordinate system. The calculation result is the cosine values corresponding to $\angle R_R R_N R_S$.

In formula (7), R_S represents the point corresponding to the reflectance value of the short-wave infrared in the coordinate system, B_M represents the point corresponding to the brightness temperature value of the mid-infrared band in the coordinate system. Similarly, $|B_M B_F|$ represents the distance between the points corresponding to the brightness temperature values of the mid-infrared band and far-infrared band in the coordinate system， $|R_S B_F|$ represents the distance between the points corresponding to the reflectance value of the short-wave infrared band and the brightness temperature value of the far-infrared band in the coordinate system. The calculation result is the cosine values corresponding to $\angle R_S B_M B_F$.

Differences in the order of magnitude of the coordinate axes are relatively large and the setting of the same distance scale values on the coordinate axis directly affect the change in the Angle slope index, thus generating different forest fire discrimination thresholds. When the ratio of the same distance scale values on the coordinate axis (y/x, ignoring units) increases, the angles $\angle R_R R_N R_S$, $\angle R_S B_M B_F$ increase，the threshold decreases, and the threshold difference also decreases; when the y/x ratio decreases, the angles $\angle R_R R_N R_S$ ， $\angle R_S B_M B_F$ decrease，the threshold increases, and the threshold difference also increases。

 doi:10.20944/preprints202410.0009.v1

When a forest fire occurs, the pixel points in the fire area show an increase in the angle $\angle R_R R_N R_S$, the angle slope index ANIR decreases, $\angle R_S B_M B_F$ decreases, the angle slope index AMIR increases, and the difference between AMIR and ANIR is used to construct the angle slope difference index, enhancing the sensitivity and accuracy of fire detection. AMNIR is defined as:

$$AMNIR = AMIR - ANIR, \tag{8}$$

Angle slope indices in Himawari-8were defined as follows：

$$ANIR = \frac{|R_3R_4|^2 + |R_4R_5|^2 - |R_3R_5|^2}{2|R_3R_4||R_4R_5|}, \tag{9}$$

$$AMIR = \frac{|R_6R_7|^2 + |R_7R_8|^2 - |R_6R_8|^2}{2|R_6R_7||R_7R_8|}, \tag{10}$$

In formula (9), R_3 and R_4 respectively represent the points in the coordinate system corresponding to the reflectance values of bands 3 and 4. $|R_3R_4|$ represents the distance between these two points in the coordinate system. Similarly, $|R_4R_5|$ represents the distance between the points corresponding to the reflectance values of bands 4 and 5, and $|R_3R_5|$ represents the distance between the points corresponding to the reflectance values of bands 3 and 5. The $ANIR$ calculation result is the cosine value corresponding to $\angle R_3R_4R_5$.

In formula (10), R_6 represents the point in the coordinate system corresponding to the reflectance value of band 6, R_7 represents the point corresponding to the brightness temperature value of band 7, and $|R_6R_7|$ represents the distance between these two points. Similarly, $|B_7R_8|$ represents the distance between the points corresponding to the brightness temperature values of bands 7 and 8, and $|R_6B_8|$ represents the distance between the points corresponding to the reflectance value of band 6 and the brightness temperature value of band 8. The $AMIR$ calculation result represents the cosine value corresponding to $\angle R_6R_7R_8$.

2. Construction of Time-series Angle slope difference index and forest fire discrimination;

The Angle Slope Difference Index is constructed based on the spectral differences between forested areas and fire points before and after a fire occurs. It is defined as follows：

$$\Delta ANIR = ANIR_{t1} - ANIR_{t2}, \tag{11}$$

$$\Delta AMIR = AMIR_{t2} - AMIR_{t1}, \tag{12}$$

$ANIR_{t1}$ and $AMIR_{t1}$ represent the angle indices of the forest before a fire, while $ANIR_{t2}$ and $ANIR_{t2}$ represent the angle indices of the forest after a fire. $\Delta ANIR$ and $\Delta AMIR$ represent the difference in the angle slope indices between the forested area and the fire point.

In actual monitoring, $ANIR_{t1}$ and $AMIR_{t1}$ represent the angle indices of the previous moment image in time-series remote sensing imagery, while $ANIR_{t2}$ and $AMIR_{t2}$ represent the angle indices of the next moment image in the time-series remote sensing imagery. $\Delta ANIR$ and $\Delta AMIR$ represent the difference in angle indices between the two scenes.

3. Decomposed 3D OTSU adaptive threshold segmentation algorithm.

To address the misjudgment of fire points in satellite imagery due to background variations in different regions, the decomposed three-dimensional OTSU algorithm is employed for adaptive threshold segmentation. This algorithm not only considers the between-class variance and the clustering within classes but also successfully decomposes the three-dimensional problem into three one-dimensional components. This reduction in dimensionality dramatically decreases the computational complexity from $O(L^3)$ to $O(L)$, significantly enhancing the computation speed and

 doi:10.20944/preprints202410.0009.v1

practical utility of the algorithm. It outperforms other segmentation algorithms in efficiency. The computation process for the decomposed three-dimensional OTSU algorithm is outlined as follows:

Let value s divide a set of discrete data into two categories (fire points target and background). For these two categories, define their inter-class distance as:

$$sb(s) = |\mu_1(s) - \mu_0(s)|, \tag{13}$$

Where $\mu_1(s)$, $\mu_0(s)$ are the mean values of the elements corresponding to their respective categories. It can be seen the larger $sb(s)$, the greater the inter-class distance, which means the target and background are more distinctly separated, resulting in better segmentation effects.

When values divide a set of discrete data into two categories, where P_i is the probability of data i occurrence, $W_0(s)$ and $W_1(s)$ respectively represent the probabilities of the two categories, and $\mu_0(s)$ and $\mu_1(s)$ are the mean values of the corresponding categories, the intra-class distances for these categories are defined as:

$$d_0(s) = \frac{\sum_{i=0}^{S} P_i|i-\mu_0(s)|}{W_0(s)}, \tag{14}$$

$$d_1(s) = \frac{\sum_{i=s+1}^{L-1} P_i|i-\mu_1(s)|}{W_1(s)}, \tag{15}$$

The overall intra-class distance for the two categories is:

$$sw(s) = W_0(s)d_0(s) + W_1(s)d_1(s), \tag{16}$$

which indicates the cohesion within each class. The best segmentation effect is achieved when the value of $sw(s)$ is minimized。

Thus, considering both the aforementioned factors, it is essential to ensure the maximum inter-class distance while also achieving the best possible cohesion within each class to obtain optimal segmentation results. Based on these requirements, upon analyzing Otsu, a new threshold determination function has been proposed, where the formula to find the threshold is:

$$G(s) = \frac{W_0(s)W_1(s)sb(s)}{sw(s)}, \tag{17}$$

The gray level corresponding to the maximum value of $G(s)$ is considered the optimal threshold S_0, that is:

$$s_0 = argmax\{G(s)\}, \tag{18}$$

For the single-channel imagery constructed using the Angle slope difference index $AMNIR$, three-dimensional OTSU adaptive threshold segmentation is applied. For the segmented anomalous target points, forest fire discrimination is conducted based on the following principles:

If $\Delta AMIR > \Delta AMIR_{Threshold}$ and $\Delta ANIR > \Delta ANIR_{Threshold}$, The potential fore point is determined.

2.2.3. Flare Removal

When the fire points were identified, it is necessary to perform flare removal to filter false fire points. The removing principle is as follows: if the reflectivity of the visible light and infrared are both greater than 0.3, and the flare angle is less than 30°, then the pixels are identified as flare. The flare angle[1] is calculated as:

$$\cos\theta_r = \cos\theta_v \cos\theta_s - \sin\theta_v \sin\theta_s \cos\psi, \tag{19}$$

Where: θ_r is the angle between the direction of the specular reflection and the vector pointing from the ground to the satellite. θ_v is the observation zenith angle, θ_s is the solar zenith angle, ψ is the relative azimuth.

2.2.4. Precision Evaluation Method

Preprints.org (www.preprints.org) | NOT PEER-REVIEWED | Posted: 1 October 2024 doi:10.20944/preprints202410.0009.v1

The accuracy rate (P), missed rate (M), and overall evaluation (F) were used to carry out the evaluation in a unified way [2]. The specific formula is as follows:

$$P = \frac{Y_y}{Y_y + Y_n}, \tag{20}$$

$$M = \frac{N_y}{Y_y + N_y}, \tag{21}$$

$$F = \frac{2P(1-M)}{1+P-M}, \tag{22}$$

where Y_y is the number of real fire points detected, Y_n is the number of falsely detected fire points; N_y is the number of missed fire points, P and M are the accuracy rate and the omission errors respectively, and F is the comprehensive evaluation index of accuracy rate and missed detection rate.

3. Results

3.1. Angle Slope Index Threshold Statistics

In the coordinate system, a y/x=500 ratio was used for threshold calculation (y is the downloaded remote sensing dataset's original values, where reflectance= true reflectance ×10000, and brightness temperature=true brightness temperature value×10). The y/x ratio in spectral line setting was around 500 when retrieving and viewing sample points in the software library, therefore 500 is used in this paper. If a y/x=1000 ratio is selected, the analysis result is not affected, but the angle difference is more obvious at 500.

The extraction of 257 fire points and 132 forest spectral curves is displayed in Figure 7. The statistical diagram shows that the spectral curves of fire point samples rise overall compared to forest samples, with a significant increase in the B7 band and a significant decrease in the B4 band, thus causing a significant increase in $\angle B3B4B5$ and a significant decrease in $\angle B6B7B8$; the brightness temperature values from B8 to B16 increase significantly, resulting in a separation from the forest spectral curves, but the degree of change is less significant than in the B7 band, and the angle change is not obvious; based on these characteristics, the Mid-Infrared Angle slope index AMIR, Near-Infrared Angle slope index ANIR, and Near-Mid Angle slope difference index AMNIR are constructed to discriminate fire points in forest fires.

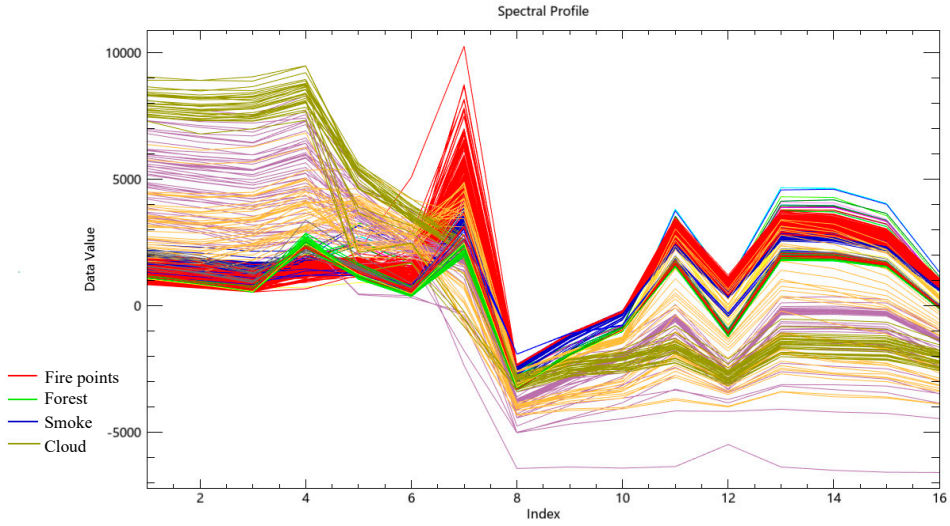

Figure 7. Spectral curve chart of forest land samples, fire point samples, smoke, and clouds .

From the selected 257 fire points and 132 forest samples, the AMIR, ANIR and AMNIR index values were calculated and statistically analyzed. As shown in Figure 8 (a) and (b), the ANIR index

Preprints.org (www.preprints.org) | NOT PEER-REVIEWED | Posted: 1 October 2024 doi:10.20944/preprints202410.0009.v1

values of fire point fluctuates within a certain range due to the complex fire environment, but overall, they still show a decreasing trend compared with forest samples; meanwhile, the AMIR values of fire points generally increase compared with forest samples.

After removing outliers, the AMIR values for fire points are above 0.96, and ANIR values are mostly below -0.5; for forest samples, the AMIR values are below 0.95, and ANIR values are above 0.5. Considering the early stages of forest fires, when the area of forest destruction is small, thermal radiation heats up slowly, and the impact of forest fire smoke on the visible light region, the discrimination formula for potential fire points is derived as follows:

$$AMIR > 0.96, \tag{23}$$

$$AMIR > 0.95 \quad and \quad ANIR < 0, \tag{24}$$

As shown in Figure 8 (c), all AMNIR values of forest samples are below 0.5, and AMNIR values of most fire points are above 1.0. Therefore, it is considered that when the regional segmentation threshold is less than 1.0, there is no fire occurrence.

From the selected 132 sample points, the $\Delta AMIR$ and $\Delta ANIR$ index values for fire points and forest pixels are statistically analyzed. As shown in Figure 8 (d) and (e), after excluding outliers, the $\Delta ANIR$ values are all above 1, and the $\Delta AMIR$ values are all above 0.03. The relative formula for fire point discrimination is as follows:

$$\Delta AMIR > 0.03 \quad and \quad \Delta ANIR > 1.0, \tag{25}$$

Preprints.org (www.preprints.org) | NOT PEER-REVIEWED | Posted: 1 October 2024 doi:10.20944/preprints202410.0009.v1

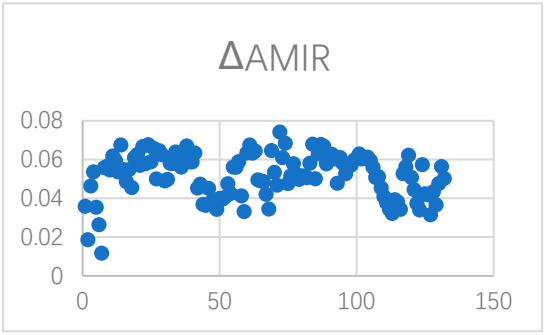

(e)

Figure 8. Statistical charts of the Angle slope indexes ANIR, AMIR, $\Delta ANIR$, $\Delta AMIR$. (a) Forest and fire point ANIR index comparison chart; (b) Fire point and forest AMIR index statistical chart; (c) Forest and fire point AMNIR index comparison chart; (d) $\Delta ANIR$ index statistical chart; (e) $\Delta AMIR$ index statistical chart.

The statistical results for the maximum, minimum, and average values of the Angle slope index and the Time-series Angle slope difference index are shown in Table 4.

Table 4. Summary of Angle Slope Index.

Index	Maximum	Minimum	Average	Variance
$\Delta ANIR$	1.8702	-0.0242	1.5594	0.1540
$\Delta AMIR$	0.0741	-0.0242	0.0517	0.0001
$ANIR_{forest}$	0.8823	0.7165	0.8210	0.0016
$ANIR_{fire}$	0.8094	-0.9999	-0.7381	0.1506
$AMIR_{forest}$	0.9453	0.9182	0.9308	0.0001
$AMIR_{fire}$	0.9937	0.9460	0.9822	0.0000
$AMNIR_{forest}$	0.2234	0.0362	0.1095	0.0017
$AMNIR_{fire}$	1.9926	0.1551	1.7108	0.0097

Note. $ANIR_{forest}$ is index ANIR of the forest samples. $ANIR_{fire}$ is index ANIR of the fire points. $AMIR_{forest}$ is index AMIR of the forest samples. $AMIR_{fire}$ is index AMIR of the fire points. $AMNIR_{forest}$ is index AMNIR of the forest samples. $AMNIR_{fire}$ is index AMNIR of the fire points.

It can be seen from Table 4 that the maximum value of index $\Delta ANIR$ is 1.8702, the minimum value is -0.0242, the mean value is 1.5594, and the minimum value deviates greatly from the mean value; The maximum value of $\Delta AMIR$ is 0.0741, the minimum value is -0.0242, the mean value is 0.0517, and the minimum value deviates greatly from the mean value; The fire point index $\Delta ANIR$ has a maximum value of 0.8094, a minimum value of -0.9999 and an average value of -0.7382, and the maximum value deviates greatly from the mean value. The maximum value of fire point index $AMNIR$ was 1.9926, the minimum value was 0.1551, and the mean value was 1.7108, the minimum value deviates greatly from the mean value. These extreme points with large deviations from the mean may be due to the low intensity and low temperature of the initial fire points, or the complex fire conditions caused by the smoke and other particles produced in the combustion process of biomass. The maximum value of forest land index $ANIR$ was 0.8823, the minimum value was 0.7165, and the mean value was 0.8210; The maximum value of forest land index $AMIR$ was 0.9453, the minimum value was 0.9182, and the mean value was 0.9308; The maximum value of fire point index $AMIR$ is 0.9937, the minimum value is 0.9460, and the average value is 0.9822; The maximum value of forest land index $AMNIR$ was 0.2234, the minimum value was 0.0362, and the mean value was 0.1095; The $ANIR$, $AMIR$, $AMNIR$ values of all forest samples, and the $AMIR$ values of fire point samples were all near the mean value, and no abnormalities were found. The variances of $\Delta ANIR$

 doi:10.20944/preprints202410.0009.v1

and fire *ANIR* are 0.15, the others are below 0.01. It showed that the stability of the fire point sample was less than that of the forest sample, and the sample was more stable in the middle infrared than in the near infrared. By comparison, the statistical results in Table 4 were consistent with those shown in Figure 8.

3.2. Forest Fire Identification Precision of Application Case

Taking Hunan Province as study area, 9 moments of the Himawari-8 satellite imagery in recent years are randomly selected as application cases for 3.2.1 Forest fire identification precision based on Angle slope index threshold (ASITR), 3.2.2 Forest fire identification precision based on the Fusion of Angle Slope Difference Index (*AMNIR*) data, Decomposed three-dimensional OTSU adaptive threshold segmentation Algorithm and ASITR (FAMN_OTSU_ASITR).

3.2.1. Forest Fire Identification Precision Based on Angle Slope Index Threshold (ASITR)

Table 5 shows the Himawari-8 satellite imagery from 2018 to 2021. These 9 moments were identified as Moment 1, Moment 2, Moment 3, Moment 4, Moment 5, Moment 6, Moment 7, Moment 8 and Moment 9.

Table 5. Application case data information.

No.	Identification	Imagery	Num. Of Gro. Tru. Fir./Pcs	Level
1	Moment 1	NC_H08_20210220_0210_R21_FLDK.06001_06001.nc	12	Level 1
2	Moment 2	NC_H08_20210119_0150_R21_FLDK.06001_06001.nc	10	Level 1
3	Moment 3	NC_H08_20210114_0410_R21_FLDK.06001_06001.nc	9	Level 1
4	Moment 4	NC_H08_20201108_0200_R21_FLDK.06001_06001.nc	5	Level 1
5	Moment 5	NC_H08_20191031_0610_R21_FLDK.06001_06001.nc	9	Level 1
6	Moment 6	NC_H08_20191001_0430_R21_FLDK.06001_06001.nc	14	Level 1
7	Moment 7	NC_H08_20190928_0320_R21_FLDK.06001_06001.nc	8	Level 1
8	Moment 8	NC_H08_20181006_0410_R21_FLDK.06001_06001.nc	7	Level 1
9	Moment 9	NC_H08_20181005_0110_R21_FLDK.06001_06001.nc	14	Level 1

Note: No.=Number. Num. of Gro. Tru. Fir.=Number of ground truth fires.

The ASITR method discriminates forest fires according to the Angle slop indices threshold obtained from forest fire points statistics. Its flow chart is shown in the left branch of the Figure 6, and the threshold determination rules follows formulas 23 to 25. The method is based on the B3B4B4 and B6B7B8 dataset of Himawari-8, and evaluated by using forest fire actual data. Forest fire identification precision of the ASITR method is shown in Table 6.

As shown in Table 6, difference between the maximum value and the minimum value of fire identification is 22.22%, forest fire identification accuracy is the smallest of 77.78% at Moment3. The accuracy of forest fire identification is above 80% at Moments 1, 2, 4, 5, 6, 7, 8, and 9. The average value of forest fire identification accuracy is 88.25%, the average value of forest fire omission error is 17.07%, and the average comprehensive evaluation value is 85.71%. Compared to the infrared radiation-based monitoring results proposed by Feng et al. [1] (with an accuracy of 0.84, a missed detection rate of 0.24, and a comprehensive evaluation value of 0.8), the accuracy has increased by 9.25%, the missed detection rate has worsened by 3.07%, and the overall evaluation index has improved by 2.62%. The increase in the missed detection rate may be due to the statistical threshold samples being collected from Australia, which is located in the subtropical region, leading to relatively higher thresholds. It is concluded that forest fire by using the ASITR method based on the B3B4B5 and B6B7B8 dataset gets the result with higher accuracy, but at the same time there is a phenomenon of forest fire omission error.

 doi:10.20944/preprints202410.0009.v1

Table 6. Precision evaluation based on the method of ASITR.

No.	Identification	Num. Of Gro.Tru. Fir./Pcs	Num. Of Fir. Mon./Pcs	Num. of Fal. Fir./Pcs	For.Fir.Ide.Acc.	For.Fir.Ide.Mis.	For.Fir.Ide.Ove.
1	Moment 1	12	10	2	83.33%	16.67%	83.33%
2	Moment 2	10	9	1	90.00%	10.00%	90.00%
3	Moment 3	9	7	2	77.78%	22.22%	77.78%
4	Moment 4	5	4	1	80.00%	20.00%	80.00%
5	Moment 5	9	7	0	100.00%	22.22%	87.50%
6	Moment 6	14	11	1	91.67%	21.43%	84.62%
7	Moment 7	8	7	0	100.00%	12.50%	93.33%
8	Moment 8	7	6	1	85.71%	14.29%	85.71%
9	Moment 9	14	12	2	85.71%	14.29%	85.71%
Ave.	—	—	—	—	88.25%	17.07%	85.33%

Note. No.=Number. Num. of Gro. Tru. Fir.=Number of ground truth fires. Num. of Fir. Mon.=Number of fires monitored. Num. of Fal. Fir.=Number of false fires. Pcs.=Pieces. For.Fir.Ide.Acc.=Forest fire identification accuracy. For.Fir.Ide.Mis.=Forest fire identification missed rate. For.Fir.Ide.Ove.=Forest fire identification overall evaluation. Ave.=Average. Num. of Gro. Tru. Fir. is derived from forest fire actual data(see section 2.1.2). Num. of Fir. Mon. is derived from the forest fire ASITR monitoring result, which represents the actual number of forest fire detected. For. Ide. Acc., Num. of Fir. Mis. And For.Fir.Ide.Ove. are calculated according to Equation(20-22)(see section 2.2.4).

3.2.2. Forest Fire Identification Precision Based on the Fusion of Angle Slope Difference Index (*AMNIR*) Data, Decomposed Three-Dimensional OTSU Adaptive Threshold Segmentation Algorithm and ASITR (FAMN_OTSU_ASITR)

The FAMN_OTSU_ASITR method discriminates forest fires by fusing Angle slope difference index (*AMNIR*) data, decomposed three-dimensional OUST adaptive threshold segmentation algorithm and the ASITR method. Its flow chart is shown in the right branch of Figure 6.

First set up windows to monitor potential forest fire points according to different regions and different environmental conditions. As shown in Figure 9, the selected study area Hunan Province was divided into 11 rows and 11 columns which contains 121 sub-regions, 18 blank windows in them. Then the sub-regions constructed from the Angle slope difference index (AMNIR) data were segmented by decomposed three-dimensional OTSU algorithm. The segmentation threshold data of each sub-region is partially shown in Figure 9. It can be seen that as the latitude increases, the threshold of potential forest fire points gradually decreases. The algorithm makes full use of the information of neighboring pixels and can be flexibly applied to regions of different latitudes.

Based on the statistical result, the segmentation thresholds are mostly below 0.2, the overall trend is that thresholds in lower latitude regions are slightly higher than those in higher latitude regions. Negative values may occur due to complex fire environments caused by smoke and heat.

According to the statistical result of Figure 8 (c) in section 3.1, if the segmentation threshold of sub-region is less than 1.0, it is considered that there is no fire occurrence.

 doi:10.20944/preprints202410.0009.v1

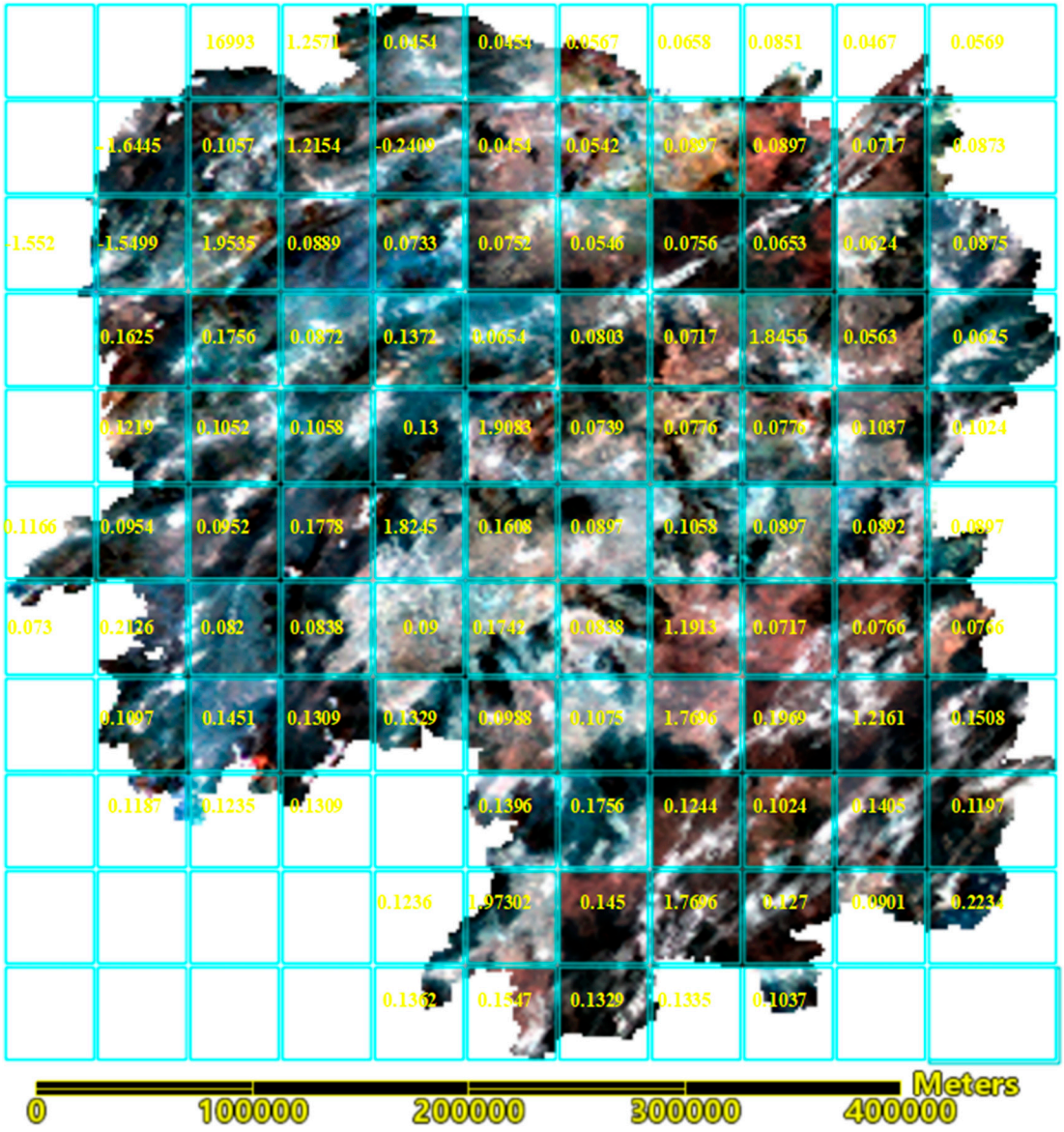

Figure 9. Identification threshold of potential forest fires on September 28, 2019, 03：20（UTC）in Hunan Province. The yellow numbers represent the potential fire threshold segmented by the decomposed 3D Otsu method.

After fusion of the Decomposed three-dimensional OTSU adaptive threshold segmentation Algorithm based on Angle slope difference index (*AMNIR*) data and the ASITR , the final precision evaluation is shown in Table 7. The result shows that the accuracy fluctuates significantly, with a maximum value of 100% and a minimum value of 71.43%, a difference of 28.57%. The average accuracy is 84.92%, slightly lower than the results of the ASITR (88.25%), but the missed detection rate is consistently lower than the ASITR. The missed detection rate at Moment 1, Moment 2, Moment 3, Moment 4, Moment 5, Moment 6, Moment 7, Moment 8, and Moment 9, are respectively 8.34%, 0%, 0%, 20%, 11.11%, 7.14%, 12.50%, 14.29%, and 7.15%, with an average reduction in missed rate of 8.95%. The overall evaluation indices are improved except for Moment 7 than the ASITR method. The results indicate that using the FAMN_OTSU_ASITR method to integrate the discrimination results of the decomposed three-dimensional OTSU adaptive threshold segmentation Algorithm with the discrimination results of the ASITR method reduces the average forest fire detection missed rate from 17.07% to 8.12%, and increases the average overall evaluation index from 85.33% to 87.85%, effectively enhancing the precision of forest fire detection.

Taking Moment 6 and Moment 7 as examples, the Spatial distribution of forest fire discrimination results based on the FAMN_OTSU_ASITR method are shown in Figure 10. The green

Preprints.org (www.preprints.org) | NOT PEER-REVIEWED | Posted: 1 October 2024 doi:10.20944/preprints202410.0009.v1

line represents the vector of Hunan Province, the red squares indicate actual data of forest fires. The yellow pentagrams represent the monitoring results based on the FAMN_OTSU_ASITR method.

Table 7. Precision evaluation based on the method of FAMN_OTSU_ASITR.

No.	Identification	Num. Of Gro.Tru. Fir./Pcs	Num. Of Fir. Mon./Pcs	Num. of Fal. Fir./Pcs	For.Fir.Ide.Acc.	For.Fir.Ide.Mis.	For.Fir.Ide.Ove.
1	Moment 1	12	11	3	78.57%	8.33%	84.62%
2	Moment 2	10	9	1	90.00%	10.00%	90.00%
3	Moment 3	9	7	2	77.78%	22.22%	77.78%
4	Moment 4	5	5	2	71.43%	0.00%	83.33%
5	Moment 5	9	8	0	100.00%	11.11%	94.12%
6	Moment 6	14	12	1	92.31%	14.29%	88.89%
7	Moment 7	8	8	2	80.00%	0.00%	88.89%
8	Moment 8	7	7	1	87.50%	0.00%	93.33%
9	Moment 9	14	13	2	86.67%	7.14%	89.66%
Ave.	—	—	—	—	86.00%	8.12%	87.85%

Note. No.=Number. Num. of Gro. Tru. Fir.=Number of ground truth fires. Num. of Fir. Mon.=Number of fires monitored. Num. of Fal. Fir.=Number of false fires. Pcs.=Pieces. For.Fir.Ide.Acc.=Forest fire identification accuracy. For.Fir.Ide.Mis.=Forest fire identification missed rate. For.Fir.Ide.Ove.=Forest fire identification overall evaluation. Ave.=Average. Num. of Gro. Tru. Fir. is derived from forest fire actual data(see section 2.1.2). Num. of Fir. Mon. is derived from the forest fire FAMN_OTSU_ASITR monitoring result, which represents the actual number of forest fire detected. For. Ide. Acc., Num. of Fir. Mis. and For.Fir.Ide.Ove. are calculated according to Equation(20-22)(see section 2.2.4).

（a） （b） （c）

Moment 6

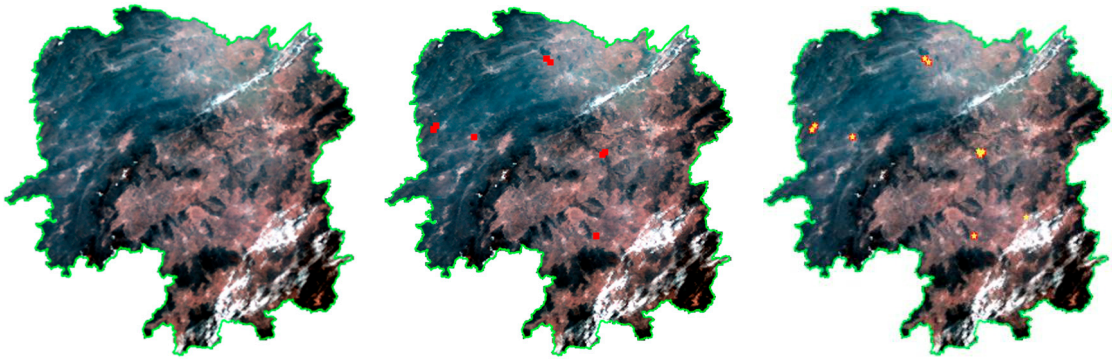

（d） （e） （f）

Moment 7

 doi:10.20944/preprints202410.0009.v1

Figure 10. Spatial distribution of forest fire discrimination results based on the FAMN_OTSU_ASITR method. The green line represents the vector of Hunan Province. The red squares indicate actual data of forest fires. The yellow pentagrams represent the monitoring results based on the FAMN_OTSU_ASITR method. Moment6 represents the moment at 04:30 UTC on October 1, 2019. Moment7 represents the moment at 03:20 UTC on September 28, 2019. As shown in Figure 10 (a), (d), a true-color image (i.e., red/green/blue) based on the Himawari-8 satellite imagery is generated as the base map. As shown in Figure 10 (b), (e), the actual data of forest fires are overlaid on Figure 10 (a), (d). As shown in Figure 10 (c), (f), the algorithm monitoring results are overlaid on Figure 10 (b), (e).

4. Discussion

In the context of future climate warming and drying leading to higher frequency and intensity of forest fires, the use of remote sensing images to detect and effectively control fires early is crucial for reducing losses. The primary goal of this paper is to address the phenomenon of missed and misclassified detections caused by fixed single-band thresholds in the forest fire discrimination process by constructing spectral Angle slope indices AMIR, ANIR, AMNIR and time-series Angle slope difference indices ΔANIR and ΔAMIR, the Angle slope indices take into account the strong correlations between different bands in the spectral images and the changes in reflectance in the visible light bands after a forest fire. It also employs a decomposed three-dimensional OTSU algorithm for threshold segmentation in different sub-regions of the forest fire monitoring area. Utilizing the high temporal resolution capabilities of the Himawari-8 satellite, recent forest fires in Hunan Province, China, were monitored. The results show that the sensitivity and accuracy of forest fire point discrimination are improved by integrating remote sensing image data from visible, near-infrared, and mid-infrared bands and using the interrelationship between different wavelengths spectral information; the time-series Angle slope difference indices utilizes changes from multi-temporal remote sensing images for forest fire point discrimination, and reduces the rate of missed detection; meanwhile, the decomposed three-dimensional OTSU algorithm based on the AMNIR data also reduces the rate of missed detections by automatically segmenting different subregions of the monitoring area.

The study of angle slope indices threshold analysis in this paper has certain temporal and spatial limitations in sample acquisition. Next steps could include collecting more fire point samples across a larger range, and incorporating cutting-edge technologies like neural networks and deep learning into forest fire detection. Advanced machine learning algorithms could bring higher accuracy to forest fire discrimination results. The high temporal resolution of Himawari-8 remote sensing data allows for near-real-time observation of fires, which is beneficial for early detection and control of fires, however, its lower spatial resolution imposes some restrictions on the identification of low-temperature, small-scale fires. Future research could improve the accuracy of forest fire discrimination by integrating multi-source remote sensing data and sub-pixel techniques.

Overall, the use of Angle slope indices, time-series Angle slope difference indices, the decomposed three-dimensional OTSU algorithm, and Himawari-8 satellite imagery for forest fire monitoring has improved identification accuracy and reduced missed detection rates, making it significantly relevant for timely monitoring and early warning of forest fires.

5. Conclusion

Using the strong correlation between spectral bands and the changes in spectral graphs caused by forest fires, new forest fire monitoring indices, the Angle slope indices, have been developed. Forest fire point discrimination based on the Angle slope index AMIR, ANIR, $\Delta AMIR$, and $\Delta ANIR$ (ASITR) shows high accuracy but also reveals some instances of missed fires. The decomposed three-dimensional OTSU algorithm is applied for adaptive threshold segmentation on sub-regions constructed from AMNIR data, combined with the Angle slope index threshold method (ASITR) for fire discrimination. This monitoring approach not only improves the accuracy of fire identification but also reduces the miss rate. The research findings have significant practical implications for early detection and control of forest fires, with the main discoveries summarized as follows:

 doi:10.20944/preprints202410.0009.v1

The occurrence of forest fires causes changes in both the reflectance of the visible light bands and the brightness temperatures of the infrared bands. Monitoring these changes simultaneously enhances sensitivity and accuracy in fire detection. The Angle slope indices are constructed based on changes in the spectral graphs of visible light reflectance and infrared brightness temperatures. Using historical data, Himawari-8 fire products (Reliability=5), visually interpreted data, 257 cloud-free fire point samples and 132 pre-disaster forest land samples in Australia were collected. The Angle slope indices values of fire points were calculated and statistically analyzed, setting threshold values for potential fire points at 0.96 or 0.95 for AMIR, 0 for ANIR, 0.03 for $\Delta AMIR$, and 1.0 for $\Delta ANIR$.

The method based on the Angle slope index threshold (ASITR) was used to monitor 88 forest fires that occurred at 9 different times during 2018-2021 in Hunan Province, China. As compared to the method proposed by Feng et al. (accuracy 0.84, miss rate 0.24, overall evaluation 0.8), accuracy increased by 9.25%, miss rate increased by 3.07%, and the overall evaluation index rose by 2.62%. The increase in the missed rate is likely attributed to the higher threshold setting which was obtained by statistical analysis of the samples from Australia, which is located in a tropical and subtropical region.

To address the difference of fire point detection thresholds under different temporal and spatial backgrounds, the decomposed three-dimensional OTSU algorithm was used for adaptive threshold segmentation based on the imagery constructed from AMNIR index data. According to the segmentation results (as shown in Example Figure 9), the thresholds were mostly below 0.2, with lower latitude regions having slightly higher thresholds than higher latitude regions. According to the statistical results of Angle slope indices, the maximum value of fire point $AMNIR$ index was 1.9926, the mean value was 1.7108, and most of the values were greater than 1.0. Therefore, if the segmentation threshold is less than 1.0, it is considered that there is no fire occurrence.

Forest fire identification based on the Fusion of Angle slope difference index ($AMNIR$) data, decomposed three-dimensional OTSU adaptive threshold segmentation Algorithm and ASITR (FAMN_OTSU_ASITR) shows large fluctuations in accuracy, with a maximum of 100% and a minimum of 71.43%, a difference of 28.57%, and an average value of 84.92%, which is higher than the method based on indices Z (the indices were constructed based on the ratio between the element value, mean value and standard deviation of the infrared bands bright temperature images.) proposed by Feng et al. [1], but slightly lower than the results from the threshold method based on the Angle slope index (ASITR) (88.25%); the missed rate is consistently lower than the ASITR method, with an average missed rate reduced by 8.95%; the overall index is 87.85%, higher than the ASITR method by 2.52%. The results show that the FAMN_OTSU_ASITR method effectively enhances the precision of forest fire detection.

6. Patents

Pingbo Liu, Gui Zhang. “Forest fire discrimination method, system, equipment and medium based on Angle slope index.” CN117333779B. 2024-04-30.

Author Contributions: Conceptualization: G.Z. and P.L.; methodology, data collection, formal analysis and writing—original draft: P.L.; funding acquisition, writing—review, comments and editing: G.Z. All authors have read and agreed to the published version of the manuscript.

Funding: This research was funded by the Scientific Research Fund of Hunan Provincial Education Department under Grant 23B0244 and 22A0194, the Science and Technology Innovation Platform and Talent Plan Project of Hunan Province under Grant 2017TP1022, the Natural Science Foundation of Hunan Province under Grant 2024JJ7645 and Field Observation and Research Station of Dongting Lake Natural Resource Ecosystem, Ministry of Natural Resources.

Data Availability Statement: The data presented in this study are available on request from the corresponding author.

Acknowledgments: We thank the Department of Emergency Management of Hunan Province for their provision of forest fire hotspot data.

Conflicts of Interest: The authors do not have conflict of interest in this study.

 doi:10.20944/preprints202410.0009.v1

References

1. Feng, H.; Zhang, G.; Tan, S.; et al. Forest fire discrimination based on Himawari-8 satellite data. *Journal of Central South University of Forestry & Technology* **2021**, *41(08)*, 75-83. [CrossRef]
2. Chinese Academy of Forestry. Available online: http://www.caf.ac.cn/info/1806/48310.htm (accessed on 6 March 2023).
3. Cai, W.; Yang, J.; Liu, Z.; et al. Forest regeneration and its influencing factors in the burnt areas of Daxing'anling Forest Region, Heilongjiang Province. *Acta Ecologica Sinica* **2012**, *32(11)*, 3303-12. [CrossRef]
4. Shi, Y.; Shan, H.; Zhang, Y.; et al. Research on forest fire monitoring of new generation of geostationary meteorological satellite. *Forest Fire Prevention* **2017**, *4*, 32-35. [CrossRef]
5. Shao, Y.; Feng, Z.; Cao, M.; et al. An ensemble model for forest fire occurrence mapping in China. *Forests* **2023**, *14(4)*, 704. [CrossRef]
6. Flannigan, M.D.; Vonder Haar, T.H. Forest fire monitoring using NOAA satellite AVHRR. *Can. J. Forest Res.* **1986**, *16*, 975–982. [CrossRef]
7. Flasse, S.P.; Ceccato, P. A contextual algorithm for AVHRR fire detection. *Int. J. Remote Sens.* **1996**, *17*, 419–424. [CrossRef]
8. Giglio, L.; Descloitres, J.; Justice,C.O.; Kaufman,Y.J. An enhanced contextual fire detection algorithm for MODIS. *Remote Sens. Environ.* **2003**, *87(nos. 2-3)*, 273-282. [CrossRef]
9. Xie, Z. Research on fire detection and exploration of auto-mated cloud detection based on Himawari8 remote sensing. PhD Thesis, University of Science and Technology of China, Beijing, 2019. [CrossRef]
10. Dozier, J. A method for satellite identification of surface temperature fields of subpixel resolution. *Remote Sens. Environ.* **1981**, *11*, 221-229. [CrossRef]
11. Miao, T. Research on the algorithm of monitoring forest fire points and estimating burn scar based on MODIS data. Master Thesis, Nanjing University of Information Science and Technology, Nanjing, 2012. [CrossRef]
12. Xu, Q.; Gu, W.; Xie, T.; et.al. Crop straw fire remote sensing monitoring and its algorithm implementation. *Remote Sensing Technology and Application* **2017**, *32(4)*, 728-733. [CrossRef]
13. Prints E.M.; Feltz, J.M.; Menzel, W.P.; et al. An overview of GOES-8 diurnal fire and smoke results for SCAR-B and 1995 fire season in South America. *J. Geophys. Res.* **1998**, *103(*D24*)*, 31821-31835. [CrossRef]
14. Riguka, S. Real-time monitoring and early warning of grassland fire based on geostationary meteorological satellite. Master of Thesis, Inner Mongolia Normal University, Huhehot, 2020. [CrossRef]
15. Giglio, L.; Descloitres, J. Justice, C.O.; et al. An enhanced contextual fire detection algorithm for MODIS. *Remote Sens. Environ.* **2003**, *87(2-3)*, 273-282. [CrossRef]
16. Giglio, L.; Csisizar, I.; Justice, C.O. Global distribution and seasonality of active fires as observed with the Terra and Aqua Moderate Resolution Imaging Spectroradiomete（MODIS）sensors. *Journal of Geophysical Research Biogeosciences* **2006**, *111(G2)*, 17-23. [CrossRef]
17. Kaufman, Y.J.; Justice, C.O.; Flynn, L.P.; et al. Potential global fire monitoring from EOS-MODIS. *J. Geophys. Res.* **1998**, *103(D24)*, 32215-32238. [CrossRef]
18. Kaufman, Y.J.; Kleidman, R.G.; King, M.D. SCAR-B fires in the tropics: Properties and remote sensing from EOS-MODIS. *J. Geophys. Res.* **1998**, *103(D24)*, 31955-31968. [CrossRef]
19. Justice, C.O.; Giglio, L.; et al. The MODIS fire products. *Remote Sens. Environ.* **2002**, *83(1-2)*, 244-262. [CrossRef]
20. Giglio, L.; Descloitre, J.; Justice, C.O.; An enhanced contextual fire detection algorithm for MODIS. *Remote Sens. Environ.* **2003**, *87(2-3)*, 273-282. [CrossRef]
21. Qin, X; Yi, H. A Method to Identify Forest Fire Based on MODIS Data. *Fire Safety Science* **2004**, *13(2)*, 83-89. [CrossRef]
22. Gao, M.; Qing, Z; Liu, S. A Study of Forest Frie Detection Based on MODIS Data. *Remote Sensing for land and Resources* **2005**, *(2)*, 60-63. [CrossRef]
23. Gong, A.; Su, Y.; Lv,X.; et al. A forest fire detection method based on MODIS. *CN106840409A*, **2017-06-13**, Beijing.
24. Xu, H.; Zhang, G.; Chu, R.; et al. Detecting forest fire omission error based on data fusion at subpixel scale. *International Journal of Applied Earth Observation and Geoinformation* **2024**, *128*, 103737. [CrossRef]
25. Xiong, D.; Tan, S.; et al. Forest fire discrimination research based on FY4 remote sensing data. *Journal of Central South University of Forestry & Technology* **2020**, *40(10)*, 42-50. [CrossRef]
26. Maeda, N.; Tonooka, H. Early stage Forest fire detection from Himawari-8 AHI images using a modified MOD14 algorithm combined with machine learning. *Sensors* **2022**, *23(1)*, 210. [CrossRef]
27. Zhang, G.; Li, B.; Luo, A self-adaptive wild fire detection algorithm with two- dimensional Otsu optimization. *Math. Problems Eng.* **2020.8**, *2020*, 1-12. [CrossRef]
28. Deng, Z.; Zhang, G. An Improved Forest Fire Monitoring Algorithm With Three-Dimensional Otsu. *IEEE Access* **2021**, *9*, 118367-118378.Otsu, N. A threshold selection method from gray-level histograms. *IEEE Transactions on Systems, Man and Cybernetics* **1979**, *9(1)*, 62-66. [CrossRef]

29. Liu, J.; Li, Wen. Two-dimensional Otsu automatic threshold segmentation method for grayscale images. *Acta Automatica Sinica.* **1993**, *19(1)*, 101-105. [CrossRef]
30. Yue, F.; Zuo, W.; Wang, K. Algorithm for selecting two-dimensional threshold of grayscale images based on decomposition. *Acta Automatica Sinica.* **2009**, *35(7)*, 1022-1027. [CrossRef]
31. Jing, X.; Li, J.; Liu, Y. An image segmentation algorithm based on three-dimensional maximum inter-class variance. *Acta Electronica Sinica.* **2003**, 09, 1281-1285. [CrossRef]
32. Schroeder, W.; Oliva, C.D.; Giglio L.; et al. The new VIIRS 375 m active fire detection data product: algorithm description and initial assessment. *Remote Sens Environ* **2014**, *143*, 85-96. [CrossRef]
33. Giglio, A.B.; Descloitres, J.; Justice, C.O.; et al. An enhanced contextual fire detection algorithm for MODIS. *Remote Sens Environ.* **2003**, *87*, 273-282. [CrossRef]
34. Prins, E.M.; Menzel, W.P. Trends in South American biomass burning detected with the GOES visible infrared spin scan radiometer atmospheric sounder from 1983 to 1991. *Journal of Geophysical Research* **1994**, *99(D8)*, 16719–16735. [CrossRef]
35. Du, P.; Liu, M.; Xu, T.; et al. Preliminary study on forest fire monitoring using Himawari-8 data. *Acta Scientiarum Naturalium Universitatis Pekinensis* **2018**, *54(06)*, 1251-1258. [CrossRef]
36. Zhao, W.; Shan, H.; Zhang, Y. Research on forest fire identification technology based on Himawari-8 geostationary satellite. *Journal of Safety and Environment* **2019**, *19(06)*, 2063-2073. [CrossRef]
37. Yan, J.; Qu, J.; Ran, M.; et al. Himawari-8 AHI fire detection in clear sky based on time-phase change. *Journal of Remote Sensing* **2020**, *24(5)*, 571-577. [CrossRef]
38. Chen, J.; Zheng W.; Liu C.; et al. Temporal sequence method for fire spot detection using Himawari-8 geostationary meteorological satellite. *National Remote Sensing Bulletin* **2021**, *25(10)*, 2095-2102. [CrossRef]
39. Zhang, P.; Guo, Q.; Guo, Q.; Chen, B.; et al. The Chinese next-generation geostationary meteorological satellite FY-4 compared with the Japanese Himawari-8/9 satellites. *Advances in Meteorological Science and Technology* **2016**, *6(1)*, 72-75. [CrossRef]
40. Dong, X.; Wei, Y.; Wang, Z. Research on the sensitivity analysis of straw burning monitoring by stationary meteorological satellite. *Heilongjiang Meteorology* **2018**, *35(1)*, 30-31. [CrossRef]
41. Jang, E.; Kang, Y.; Im, J.; Lee, D.W.; Yoon, J.; Kim, S.K. Detection and Monitoring of Forest Fires Using Himawari-8 Geostationary Satellite Data in South Korea. *Remote Sens.* **2019**, *11*, 271. [CrossRef]
42. Koltunov, A.; Ustin, S.L.; Quayle, B.; Schwind, B.; Ambrosia, V.; Li, W. The development and first validation of the GOES Early Fire Detection (GOES-EFD) algorithm. *Remote Sens. Environ.* **2016**, *184*, 436–453. [CrossRef]
43. Filizzola, C.; Corrado, R.; Marchese, F.; et al. RST-FIRES, an exportable algorithm for early fire detection and monitoring: Description, implementation, and field validation in the case of the MSG-SEVIRI sensor. *Remote Sens. Environ.* **2016**, *186*, 196-216. [CrossRef]
44. Di Biase, V.; Laneve, G. Geostationary Sensor Based Forest Fire Detection and Monitoring: An Improved Version of the SFIDE Algorithm. *Remote Sens.* 2018, 10, 741. [CrossRef]
45. Zhang, J.; Zhang, W.; Feng, J.; et al. Research on MODIS fire point monitoring algorithm based on brightness temperature-vegetation index-aerosol optical thickness. *Remote Sensing Technology and Application* **2016**, *31(05)*, 886-892. [CrossRef]
46. Xu, H.; Zhang, G.; Zhou, Z.; et al. Forest fire monitoring and positioning improvement at subpixel level: application to himawari-8 fire products. *Remote Sensing* **2022**, *14(10)*, 2460. [CrossRef]
47. Zhou, W.; Tang, B.H.; He Z.W.; et al. Identification of forest fire points under clear sky conditions with Himawari-8 satellite data. *International Journal of Remote Sensing* **2024**, *45(1)*, 214-234. [CrossRef]
48. Wooster, M.J.; Roberts, G.; Freeborn,P.H.; et al. LSA SAF Meteosat FRP products–Part 1: Algorithms, product contents, and analysis. *Atmospheric Chemistry and Physics* **2015**, *15(22)*, 13217-13239. [CrossRef]
49. Pan, J.; Xing, L.X.; Wen J.C.; Meng T.; Jiang, L.J. Inversion method studyon short wave infrared remote sensing data high temperature surface feature temperature. *Proc. 2nd Int. Congr. Image Signal Process.* **2009**, *10*, 1-4. [CrossRef]
50. Han, C.; Yang, Q.; He, X.; et al. Research on fire point identification algorithm based on Himawari-8 satellite. *Remote Sensing Technology and Application.* **2023**, *38(01)*, 173-181. [CrossRef]
51. The People's Government of Hunan Province. Available online: https://www.hunan.gov.cn/hnszf/jxxx/hngk/hngk.html (accessed on 22 9 2024).
52. The forestry Department of Hunan Province. Available online: http://lyj.hunan.gov.cn/lyj/ztzl/lshn_77586/202303/t20230306_29264640.html (accessed on 22 9 2024).